Scientific Reports

https://doi.org/10.1038/s41598-026-41676-z

Article in Press

Enhanced design of a photonic crystal biosensor for early cervical cancer detection using refractive index variation and neural network classification

Received: 26 June 2025

Accepted: 23 February 2026

Published online: 26 February 2026

Cite this article as: Karami P., Yahya S.I., Roshani S. *et al.* Enhanced design of a photonic crystal biosensor for early cervical cancer detection using refractive index variation and neural network classification. *Sci Rep* (2026). https://doi.org/10.1038/s41598-026-41676-z

Pouya Karami, Salah I. Yahya, Saeed Roshani, Fariborz Parandin & Sobhan Roshani

Enhanced Design of a Photonic Crystal Biosensor for Early Cervical Cancer Detection Using Refractive Index Variation and Neural Network Classification

Pouya Karami[1], Salah I. Yahya[2], Saeed Roshani[1*], Fariborz Parandin[1], and Sobhan Roshani[1*]

1 Department of Electrical Engineering, Ker.C., Islamic Azad University, Kermanshah, Iran
2 Department of Computer Technology Engineering, College of Technical Engineering, Al-Hadba University, Mosul, Iraq
* Correspondence: Sobhan Roshani: s.roshani@iau.ac.ir; Saeed Roshani: s_roshani@iau.ac.ir

Abstract: This study introduces a new optical sensor designed to help detect cervical cancer early, using light and special materials called photonic crystals. The sensor has been built using a simple grid of tiny silicon rods that guide light through a small pathway. When this light passes through different types of cervical tissue (healthy, HPV-infected, or cancerous) it changes slightly, de-pending on the tissue's properties. These changes help to identify the type of tissue without needing any dyes or labels. A key innovation of the proposed work is considering the impact of temperature on sensor performance, while previous studies have ignored temperature effects. Since temperature can affect how tissue interacts with light, we tested the sensor at four different temperatures (10°C, 25°C, 45°C, and 60°C) to make sure it works well in different environments. The sensor works best at 25°C, but it still performs reliably at other temperatures. The results show that this sensor is highly accurate, sensitive, and can detect even tiny differences in tissue. To enhance the classification of tissue types, an artificial neural network (ANN) was trained using key optical features from the sensor, achieving over 91% accuracy. It also has a simple design that makes it easier to build and use in real-world medical settings. Overall, this sensor has strong potential for non-invasive, fast, and reliable cervical cancer screening.

Keywords: Cervical Cancer Detection, HPV Biosensing, Refractive Index Sensing, Optical Biosensor, Photonic Crystal Sensor, Temperature Compensation,

1. Introduction

Cervical cancer is one of the most common cancers among women. If not diagnosed early, it can lead to serious complications and lower survival rates [1]. The main cause of this disease is usually a persistent infection with the human papillomavirus (HPV), which leads to cellular changes and eventually the development of cancer in the cervix [2]. Current diagnostic methods, such as Pap smear tests, colposcopy, and molecular tests, while highly accurate, face challenges like high costs, the need for advanced equipment, long processing times, and limited ability for rapid, real-time detection [3].

Recently, researchers have turned their attention to optical biosensors based on

photonic crystals (PhC) as a novel, accurate, and non-invasive approach for detecting cervical cancer[4]. In simple terms, photonic crystals are structures made of two or more materials with different refractive indices arranged in a repeating pattern [5]. These structures can control and direct the flow of light in specific ways. Key advantages of photonic crystals include the ability to guide light precisely and to miniaturize optical circuits. This has led to their use in designing logic gates, multiplexers, other digital logic circuits, and optical sensors [6].
Two-dimensional photonic crystals and photonic crystal fibers are widely used because these structures offer high sensitivity and a high Q-factor. Compared with other optical platforms, photonic crystals are better suited for building optical sensors and often deliver stronger performance. This makes research on photonic crystals and their applications, especially in optical sensing, both well-justified and necessary [7, 8].

Due to their ability to manipulate light, photonic crystals are ideal for detecting even small changes in the refractive index of their environment [9-12]. Recent studies on 2D photonic crystal applications are provided, such as [13], which used 2D photonic crystals to implement an ultra-fast optical perceptron; [14], which realized an optical XOR logic gate using 2D photonic crystals together with an artificial neural network (ANN) and particle swarm optimization (PSO); and [15], which employed a machine-learning ANN to estimate the dispersion characteristics of slotted photonic crystal waveguides (SPCW) for any chosen set of structural parameters. The machine-learning approach in [15] provides much faster solutions to the underlying 3D eigenvalue problems than conventional plane-wave expansion (PWE) simulations, which typically require significant computing time.

In an optical sensor, the presence of target molecules (such as cancer-related biomarker proteins) changes the surrounding refractive index. This change causes a shift in the resonance wavelength and alters the sensor's spectral response. Compared to electrical and chemical methods, photonic crystal-based sensors offer several advantages: high sensitivity, label-free detection (no need for biological markers), fast response times, and the ability to integrate easily with photonic integrated circuits (PICs) [16].
In previous studies on the detection of cervical cancer and HPV, such as [17], photonic crystal fibers were employed for sensor implementation. Similarly, in [18], optical fibers were used to detect infectious epidemic viruses. In [19], two-dimensional photonic crystals composed of silicon rods in air were utilized for cancer detection, where two waveguide paths introduced the light and a resonant ring structure in the center enabled cancer diagnosis. In [20], photonic crystals were applied for leukemia detection, employing a waveguide path and a resonator to form the sensor structure. In [21], a photonic crystal structure composed of silicon rods in an air substrate was utilized to realize an optical sensor for leukemia detection. The input laser light enters the structure through a waveguide formed by removing a number of rods, interacts with the region containing cancerous cells, and then exits the structure via the waveguide. Outside the structure, changes in the resonance wavelength of the output light are measured relative to a reference, enabling the identification of the cancer type.

Photonic crystal-based nanocavity sensors have demonstrated remarkable potential in early cancer detection by providing ultra-high refractive index sensitivity and low detection limits, allowing for accurate discrimination among different cancer types [22]. Similarly, in the field of defense and environmental monitoring, advanced PCF sensors have been designed to detect highly toxic nerve agents within the terahertz spectrum, achieving exceptional sensitivity and minimal optical loss [23]. Beyond these applications, PCF-based biosensors have also shown great promise in identifying viral infections with high reliability and sensitivity, further emphasizing their biomedical significance [24]. Collectively, these advancements highlight the versatility and transformative potential of photonic crystal technologies in enabling compact, cost-effective, and real-time sensing systems for global healthcare, security, and environmental safety.

In [22], a 2D photonic crystal optical sensor based on dielectric rods in air with a nanocavity resonator was optimized to detect six cancers (including cervical cancer), reporting standout results. In [21], a 2D PhC waveguide–cavity sensor for early detection of three cancers, including cervical cancer, achieved high sensitivity with a compact footprint. Study [25] presented another 2D PhC design using silicon rods in air and three ring resonators, reaching high sensitivity. Similarly, in [26], a hollow-core photonic crystal fiber was designed for detecting blood components in the terahertz region, with performance evaluated in terms of relative sensitivity, confinement loss, and effective area. In [27], a photonic crystal fiber was proposed for measuring different concentrations of sulfuric acid over the 0.8–1.8 µm wavelength range, focusing on parameters such as sensitivity, birefringence, and loss. Both works concentrate on waveguiding characteristics and refractive-index variations of the analytes and do not address temperature-dependent behavior of biological tissues or medical diagnostic modeling. The presented work in [28] proposes a rectangular-core PCF for amino acid detection with high sensitivity, but the structure is complex, restricted to THz operation, and lacks temperature and machine-learning considerations. Also study [29] presents a square-core PCF for petrochemical sensing that is non-biological and not transferable to cancer detection. In contrast, our study is, to our knowledge, the first to model temperature-dependent refractive index changes of cervical tissue at 1.55 µm and to combine the sensor outputs with an ANN. This approach improves accuracy and robustness under realistic conditions and enables intelligent, automated discrimination among healthy, HPV-infected, and cancerous tissues.

In this study, we have designed and simulated an optical biosensor based on a two-dimensional (2D) photonic crystal (PhC) for detecting cervical cancer. A key innovation of our work is considering the impact of temperature on sensor performance. While many previous studies have ignored temperature effects, we show that temperature changes can significantly influence the refractive index and, in turn, the sensor's diagnostic accuracy. Therefore, we evaluated the sensor's performance at four different temperatures (10°C, 25°C, 45°C, and 60°C).

Additionally, unlike some previous studies that used visible light wavelengths, our sensor operates in the telecommunication wavelength range of 1.55 micrometers (C-band). This spectral range is ideal because it offers minimal loss in silicon waveguides and facilitates integration with on-chip photonic systems [30, 31].

To assess the sensor's performance, we modeled the refractive indices of three types

of tissue: healthy tissue, HPV-infected tissue, and cancerous cervical tissue. We then calculated the sensitivity (S), quality factor (Q), and limit of detection (LOD). Our results show that the proposed design can detect very small changes in refractive index with high accuracy.

Another important feature of the proposed design is its structural simplicity and ease of implementation in integrated optical circuits. While many photonic sensors rely on complex resonator structures or multilayer nanostructures, our design offers a simple, compact structure that supports mass production and practical application [32].

Overall, the results of this study demonstrate that the proposed sensor not only provides highly accurate detection of cervical cancer through refractive index changes but also maintains stable performance across different temperatures. These features make it a strong candidate for early, non-invasive diagnosis of cervical cancer in clinical and laboratory environments. Figure 1 illustrates the conceptual development of the proposed biosensor. The structure is based on two-dimensional crystal photonics. The sensor enables precise detection of spectral changes associated with biological samples.

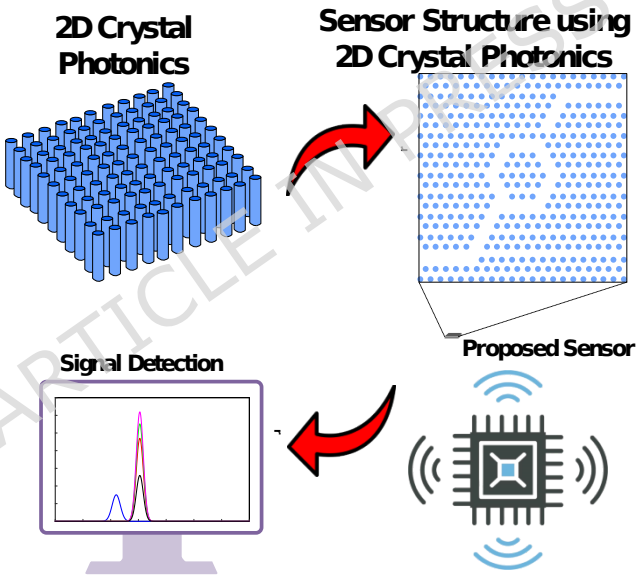

Figure 1. Conceptual diagram of the proposed biosensor system based on 2D crystal photonic structures.

2. Design of the Proposed Structure for a Fully Optical Cervical Cancer Sensor

In this study, a 2D PhC structure has been designed to develop a fully optical, label-free sensor for cervical cancer detection. The structure consists of a 21×21 hexagonal lattice formed by silicon rods embedded in an air background. The lattice constant (a), which is the distance between adjacent rods, is set at 0.6 μm. The radius (R) of each silicon rod is 0.12 μm. The refractive index of the background (air) is $n_1 = 1$, while the refractive index of the silicon rods is $n_2 = 3.46$. A total of 21 rods are placed along each side of the hexagonal array, forming a 21×21 structure.

As illustrated in Figure 2, a photonic bandgap for the transverse magnetic (TM) mode is created within the structure. Based on the simulation results, the photonic bandgap appears in two wavelength ranges: 0.813 μm < λ < 0.835 μm and 1.42 μm < λ < 2.14 μm . Wavelengths within these intervals are prohibited from propagating through the structure, effectively confining the light outside these bands. For the sensor operation, the laser wavelength is set at 1.55 μm, and the light is modeled with a Gaussian beam profile. The choice of 1.55 μm is intentional, as it corresponds to a standard telecommunication wavelength, characterized by low loss in optical fiber systems and high compatibility with integrated photonic circuits.

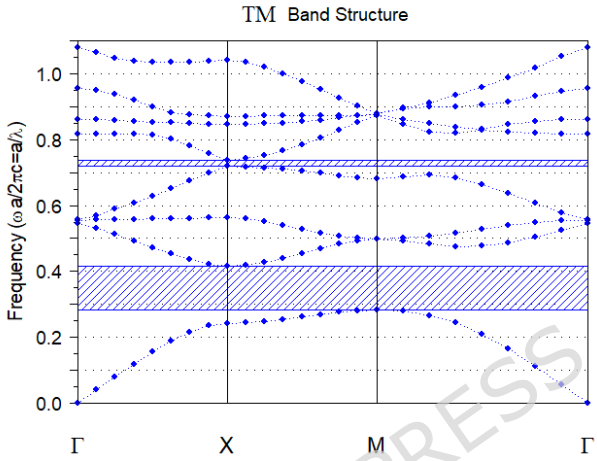

Figure 2. Normalized photonic band gap diagram in TM mode.

Figure 3 presents the structure of the proposed sensor. As shown, by removing a number of silicon rods, a waveguide path is created to guide the laser light toward the sensing region. After interacting with the sensing region, the light continues through the waveguide to the output for measurement.

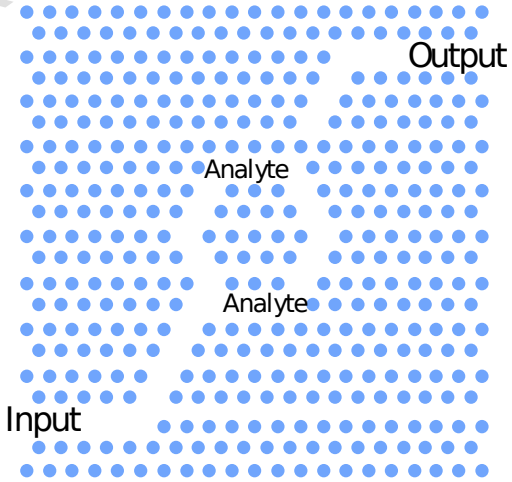

Figure 3. Structure of the proposed sensor.

2.1. Analysis of structural stability for the proposed photonic-crystal sensor

To choose the best structure for a 2D photonic-crystal sensor, four different configurations were designed and simulated (shown in Fig. 4). The quality factor (Q)

and FWHM are two key parameters in optical sensors.
In Fig. 4a, the structure uses two waveguides (for input and output) and a diamond-shaped resonator at the center (the analysis region). The footprint is compact, 76 μm², and the output peak has FWHM = 18 nm with Q = 89. In Fig. 4b, the structure again has two waveguides and a central diamond resonator (cell analysis region). The footprint is 120 μm², and the output shows FWHM = 0.7 nm with Q = 2142. In Fig. 4c, the structure has two waveguides and a ring resonator at the center (cell analysis region). The footprint is 120 μm², and the output shows FWHM = 0.7 nm with Q = 2362. Finally, Fig. 4d is the structure we propose for realizing the optical sensor to distinguish healthy and cancerous cells. We chose it because it is the optimal configuration with FWHM = 0.3 nm, Q = 5271, and a footprint of 120 μm².

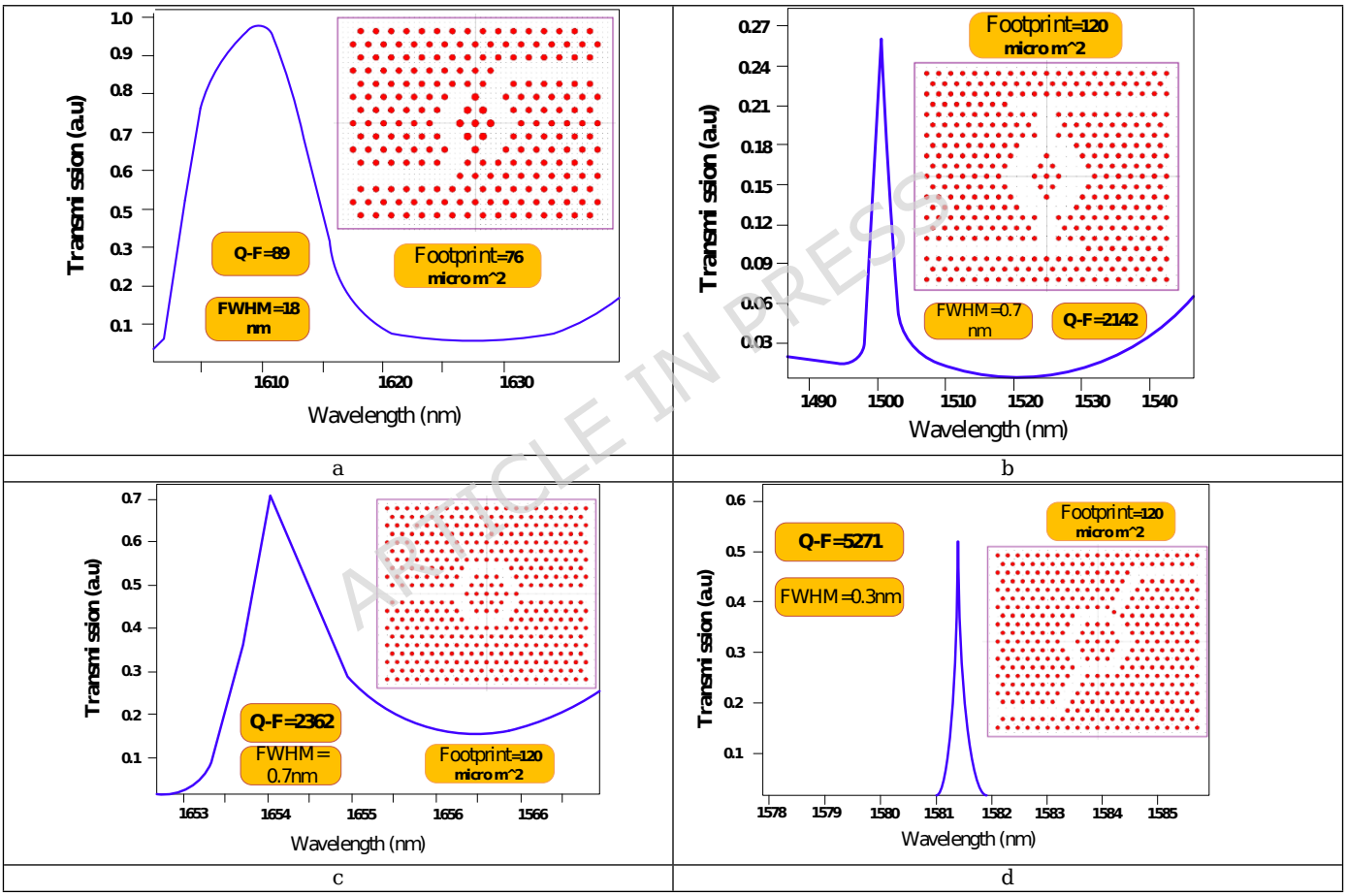

Figure 4. Different structural configurations with varying sizes used to find the optimal design for realizing a photonic-crystal sensor to detect cervical cancer cells.

Figure 5 shows how the photonic bandgap changes with the rod radius. As seen in Fig. 5, a radius of 120 nm provides a suitable bandgap that covers 1550 nm. Increasing the rod radius makes the bandgap slightly wider and shifts it toward longer wavelengths. Figure 6 presents the spectral response and the corresponding FWHM and Q-factor for different resonator-rod radii. As shown in Figure 6, the optimal radius

for the resonator rods is R = 120 nm.

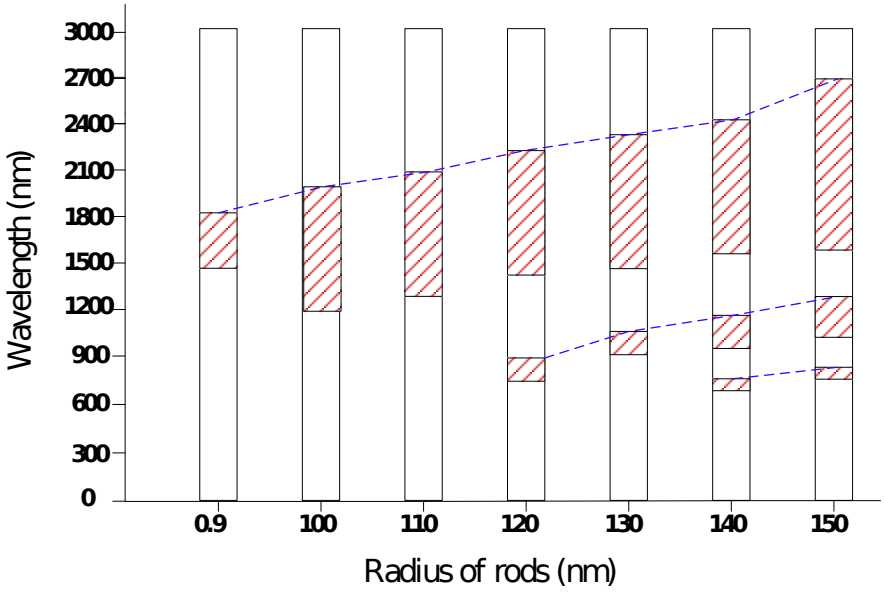

Figure 5. Changes in the photonic bandgap versus the radius of the structure's rods.

One of the biggest practical challenges for photonic-crystal optical sensors is fabrication errors during nanoscale manufacturing. Because the sensor final performance depends directly on the stability of these parameters, a careful analysis of fabrication errors is essential to judge how reliable the design will be in practice. In this study, to test the stability of the proposed structure, we varied the photonic-crystal rod radius from 90 to 150 nm and evaluated its effect on the photonic bandgap and the sensor optical parameters. Numerical results show that as the rod radius increases, the structure effective refractive index rises and the resonance wavelength gradually shifts to longer wavelengths (red-shift) as shown in Fig. 7c. This behavior is almost linear and stable for radii 90–130 nm. However, for radii above 130 nm, strong instability appears in the resonance, because the mode moves out of the photonic bandgap and optical losses increase.

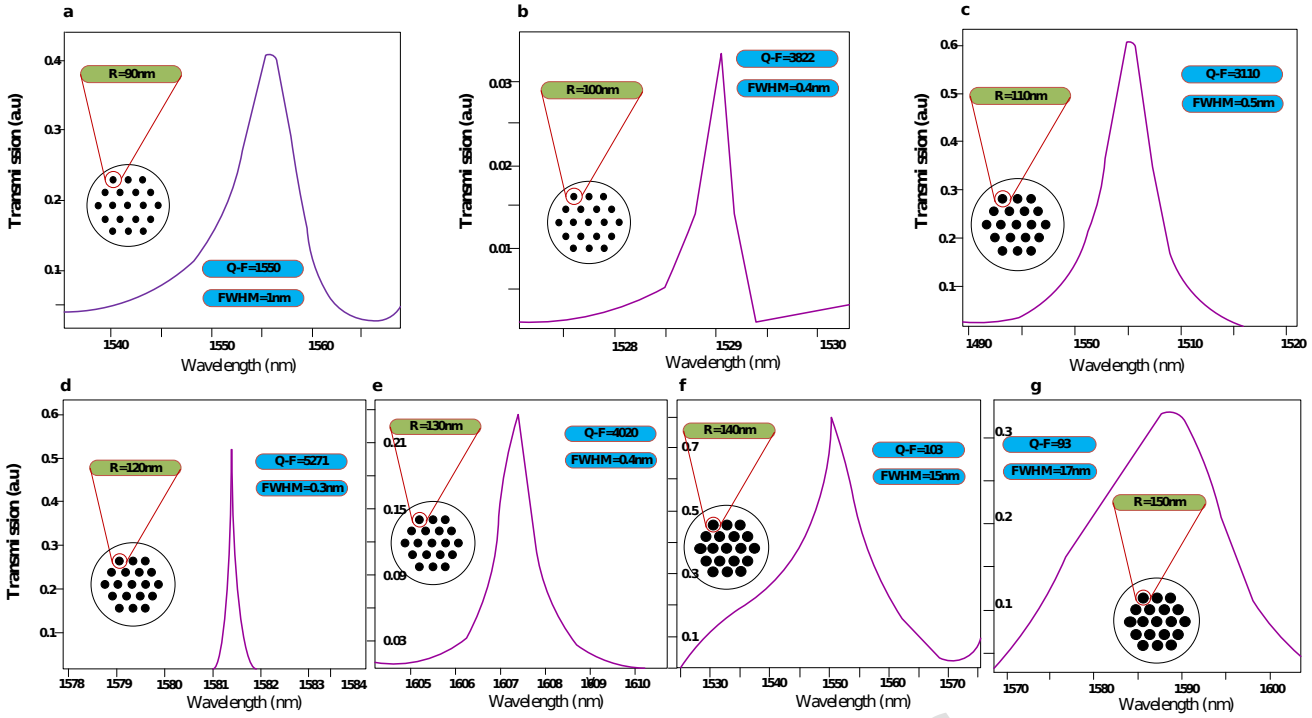

Figure 6. Spectral responses of the structure for different radii of the resonator rods.

Based on the simulations shown in Figs. 6 and 5, the highest stability and optimal performance occur at a radius of R = 120 nm. At this point, the structure reaches its maximum Q-factor of 5271, its minimum FWHM of 0.3 nm, and a resonance wavelength of 1581 nm. The photonic bandgap is also widest and most stable here. In contrast, at larger radii (especially 140 and 150 nm), the resonance linewidth increases sharply and the Q-factor drops below 150, indicating mode decay and stronger leakage.

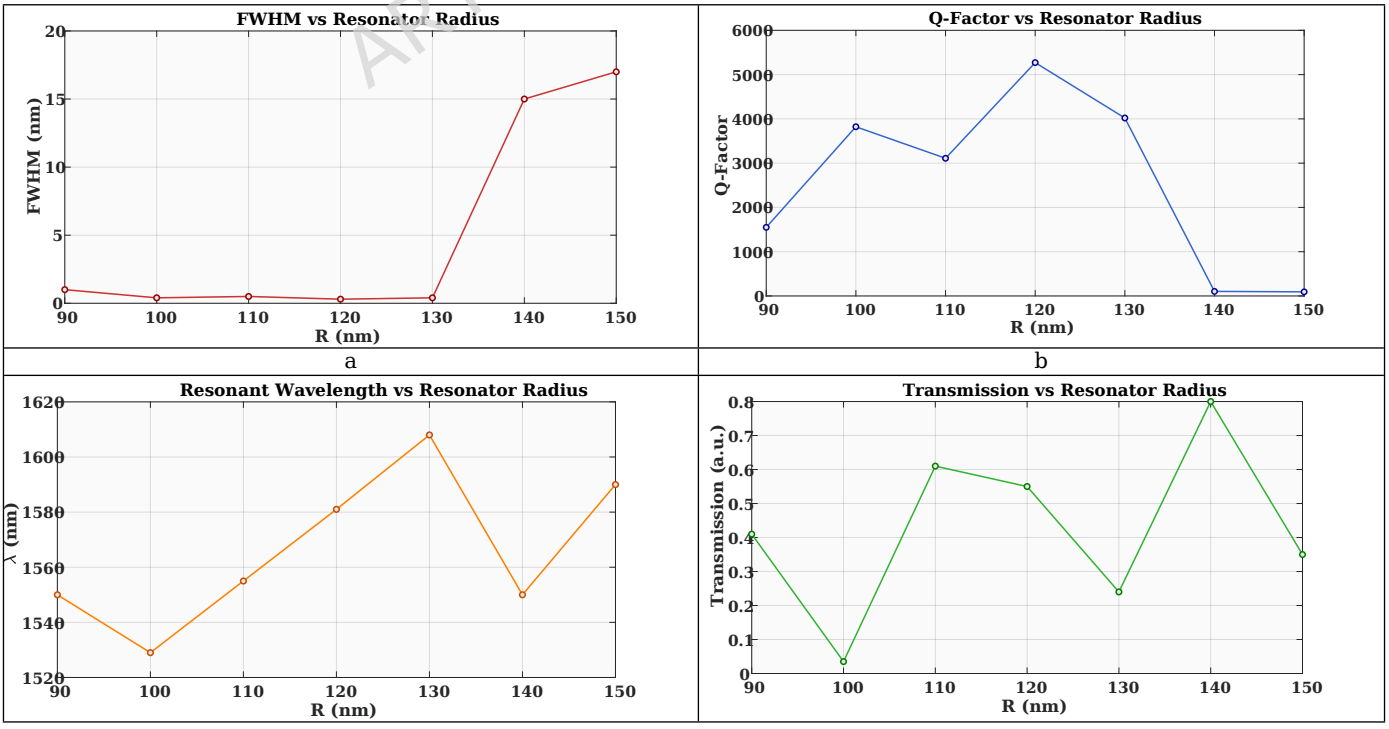

c	d

Figure 7. Values of FWHM, Q-factor, transmission, and the resonance wavelength of the proposed optical sensor versus different radii of the resonator rods.

From the photonic bandgap perspective, the results shown in Fig. 5 indicate that in the optimal range (R = 110–130 nm), the bandgap width is maximized to cover the sensor's operating wavelength (1550 nm), and the structure shows resistance to small fabrication errors (the results shown in Fig. 7a-7b-7c-7d). However, when the rod radius exceeds this range, the bandgaps gradually overlap, and new modes appear at the band edges, causing interference with the main resonance and sudden changes in optical parameters.

2.2. Proposed sensor structure

The overall working principle of the sensor is illustrated in Figure 8. As seen, light from a single-mode optical fiber is injected into the 2D PhC structure. The injected light travels through the waveguide toward the sensing area, where it interacts with the material under analysis. When the light encounters the sensing region, any change in the refractive index leads to a shift in the resonance wavelength (λ_0). After interaction, the light continues through the waveguide and exits the structure. The outgoing light is then collected by another single-mode fiber and directed into a spectrometer. The resulting output spectrum is displayed on a monitor for analysis. One of the significant advantages of this design is its structural simplicity. As clearly visible in the sensor structure, no additional defect rods are introduced, which greatly simplifies the fabrication process and avoids unnecessary complexity.

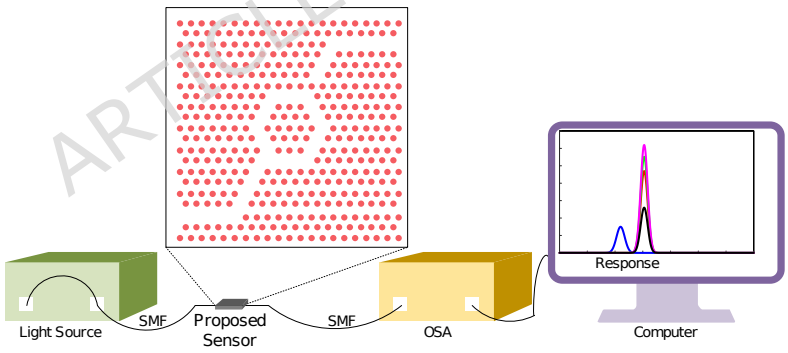

Figure 8. Schematic representation of the proposed photonic crystal-based optical sensor.

Additionally, Figure 9 illustrates the optical power distribution within the structure, showing how the light travels through the waveguide, interacts with the sensing region, and reaches the output port.

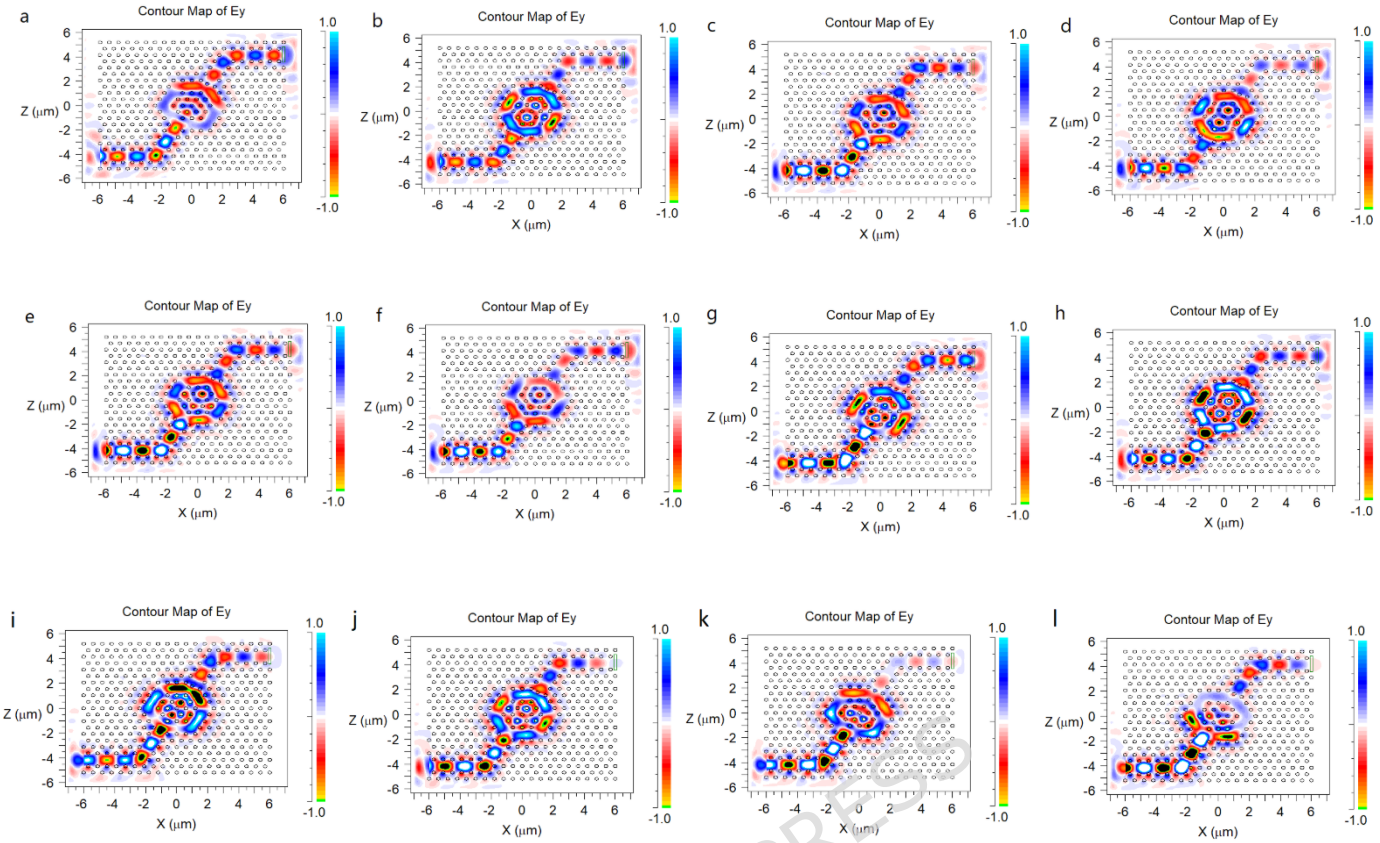

Figure 9. Optical power distribution in the sensor structure.

Figure 9 shows the contour maps of the Ey component of the electric field, representing the optical power distribution within the proposed photonic crystal sensor. Subfigures (a), (c), (e), and (g) illustrate the distribution for HPV-infected (pre-cancerous) tissue at temperatures of 10°C, 25°C, 45°C, and 60°C, respectively, while subfigures (b), (d), (f), and (h) correspond to cancerous tissue at the same temperature points. The color scale, ranging from -1 (blue) to +1 (red), indicates the normalized amplitude of the Ey field. As observed, variations in temperature and tissue type cause noticeable changes in the reflection and resonance patterns due to shifts in the refractive index at the sensing region. The differences in field concentration and propagation between HPV-infected and cancerous tissues highlight the high sensitivity and effectiveness of the proposed sensor in distinguishing between different tissue types. For a better comparison between the cancerous and precancerous states with the healthy (reference) state, the light production graphs in the reference state structure at temperatures of 10°C, 25°C, 45°C, and 60°C are shown in Figures 9-i, 9-j, 9-k, and 9-l, respectively.

2.3. Refractive Index Variation in Cervical Tissue with Temperature at 1.55μm

The refractive index of biological tissues, including cervical tissue, is influenced by various factors, with temperature being one of the key contributors. Temperature changes can affect the tissue's refractive index by altering factors such as tissue density, molecular structure, and intracellular water content. Understanding how the refractive index changes with temperature is essential for designing accurate optical biosensors, particularly for detecting diseases like cervical cancer.

This section presents a theoretical model and the calculated refractive index values for cervical tissue at different temperatures: 10°C, 25°C, 45°C, and 60°C. A linear model can be used to approximate how the refractive index of biological tissues changes with temperature, as shown below:

$$n(T) = n(T_{ref}) + \frac{dn}{dT} \cdot (T - T_{ref}) \quad (1)$$

In Equation (1), the n(T) is the refractive index at temperature T, and the $n(T_{ref})$ is the refractive index at a reference temperature T_{ref} (here, $T_{ref} = 25°C$). Also, the dn/dT is the temperature coefficient of the refractive index (measured in 1/°C), which indicates how much the refractive index changes for each degree change in temperature, and the T is the target temperature in °C. For soft biological tissues, the temperature coefficient dn/dT is usually small but still important enough to affect optical sensing. Based on experimental studies, the following values of dn/dT were used for different tissue types.

The temperature coefficients of refractive index (dn/dT) for different cervical tissue types are as follows: healthy tissue has a coefficient of 1.2×10^{-4} per °C, HPV-infected (pre-cancerous) tissue has 1.3×10^{-4} per °C, and cancerous tissue has the highest coefficient at 1.5×10^{-4}per °C. The refractive index at different temperatures was computed using Equation (2).

$$n(T) = n(T_{ref}) + \frac{dn}{dT} \cdot (T - 25) \quad (2)$$

To calculate the refractive index of different cervical tissues at the operating wavelength of 1.55 µm, baseline data were extracted from several previous numerical studies (fitted values) and simulations related to optical and photonic sensors for biological tissues [33-37]. In these sources, approximate refractive index values for healthy, HPV-infected, and cancerous tissues were reported, based on optical modeling rather than experimental measurements. Since the exact n value at 1.55 µm was not explicitly available in these studies, the reported curves of refractive index variations with wavelength in the range of 0.8 µm to 2 µm were fitted using the Sellmeier equation (Equation 3) in MATLAB to extract the n value at the sensor's operating wavelength. The used equation is written in Equation (3).

$$n^2(\lambda) = 1 + \frac{B_1\ \lambda^2}{\lambda^2 - C_1} + \frac{B_2\ \lambda^2}{\lambda^2 - C_2} \quad (3)$$

In Equation (3), λ is in micrometers, and the coefficients Ci, Bi are determined by curve fitting to the available numerical data. The fitting was done using the least squares method, and an $R^2 > 0.995$ was achieved for all three tissue types. Using the coefficients from Table 1, the refractive index for each tissue type at 1.55 µm was calculated. Then, to account for the temperature effect, Equations (1) and (2) were used to update n(T) at 10°C, 25°C, 45°C, and 60°C. As a result, the final reported refractive index values in Table 2 are based on numerical modeling and the Sellmeier

equation fit to the previous simulation data, rather than direct experimental data. The Sellmeier coefficients listed in Table 1 (25℃) were obtained by fitting the two-term Sellmeier dispersion relation to the reported refractive index data of cervical tissues from previous numerical photonic studies [33-37]. The fitted parameters were then slightly tuned to reproduce the exact refractive index values used in this work at λ = 1.55 µm (n = 1.3456, 1.3460, and 1.3471 for healthy, HPV-infected, and cancerous tissues, respectively). The dispersion shape was preserved by keeping C_1 and C_2 constant. In all cases, the coefficient of determination exceeded 0.995, confirming the accuracy of the fit.

Table 1. Coefficients obtained from the Sellmeier model fitting for three types of cervical tissues.

Tissue Type	B_1	C_1	B_2	C_2	R^2
Healthy Tissue Reference)	0.705	0.0081	0.101	0.0532	0.997
HPV-Infected (Pre-Cancerous) Tissue	0.701	0.0079	0.106	0.0508	0.996
Cancerous Tissue	0.698	0.0076	0.112	0.0473	0.995

Table 2. Refractive index values of different cervical tissue types at various temperatures (10°C, 25°C, 45°C, and 60°C) at 1.55µm.

Tissue Type	10℃	25℃	45℃	60℃
Healthy Tissue Reference)	1.3438	1.3456	1.3480	1.3498
HPV-Infected (Pre-Cancerous) Tissue	1.3440	1.3460	1.3486	1.3505
Cancerous Tissue	1.3449	1.3471	1.3501	1.3524

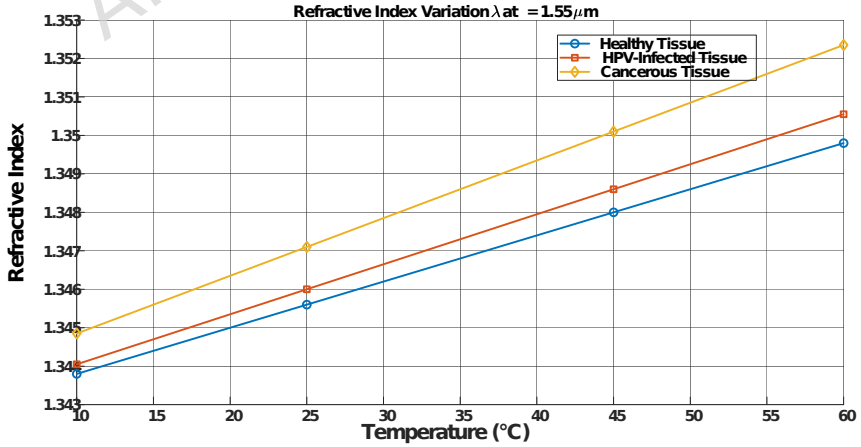

Figure 10. Change in refractive index with temperature for three types of tissue (healthy tissue, HPV-infected tissue, and cancerous cervical tissue)

Figure 10. shows the changes in the refractive index for three types of tissue at different temperatures, based on the calculations discussed above. As shown in the figure, the refractive index for these tissues increases with rising temperature. The

simulations were performed for the refractive index values of these three tissue types at 10°C, 25°C, 45°C, and 60°C.

2.3. Key Parameters in Photonic Crystal Optical Sensors

In optical sensors based on photonic crystals, sensitivity is a key parameter that shows how much the resonance wavelength shifts when the refractive index changes. It is defined by the equation $S=\Delta\lambda/\Delta n$, where $\Delta\lambda$ is the change in the resonance wavelength and Δn is the change in the refractive index [5].

Another important parameter is the full width at half maximum (FWHM), which refers to the wavelength range over which the sensor's response is at least half of its maximum value. This parameter is commonly measured in nanometers (nm) and is related to the sensor's precision and resolution. A smaller FWHM value means the sensor can detect smaller changes in the refractive index more accurately.

Figure 11 illustrates the reference waveform of the proposed structure at a temperature of 10 ℃. This waveform serves as a baseline for comparison with waveforms obtained under different conditions, such as varying temperatures or refractive indices. Analyzing this reference helps evaluate the sensor's performance and sensitivity to external changes.

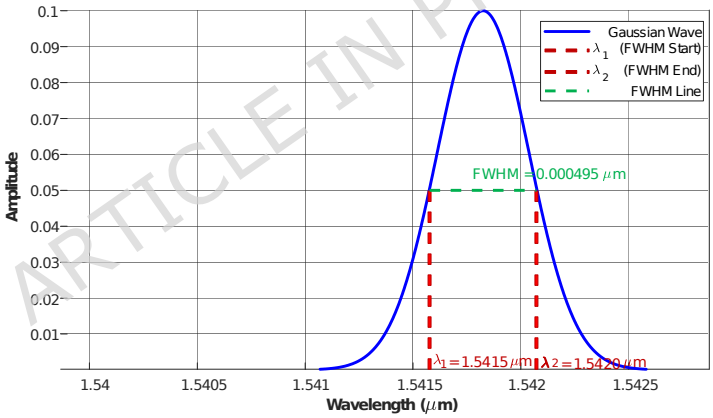

Figure 11. Reference waveform of the structure at a temperature of 10 ℃.

The Figure of Merit (FOM) is a key parameter that reflects the sensor's ability to detect very small changes in the refractive index. It is expressed in units of RIU^{-1} (refractive index unit inverse). As shown in Equation 4, FOM is calculated by dividing the sensitivity (S) by the full width at half maximum (FWHM), where S represents the sensor's sensitivity and FWHM denotes the bandwidth at half of the peak response.

$$FOM = \frac{S}{FWHM} \tag{4}$$

The Quality Factor (Q) is an important parameter that reflects the performance and precision of an optical system, such as a resonator or sensor. It is closely related to the system's bandwidth and its ability to store energy in resonance mode. A higher Q value indicates that the system can retain more energy at resonance and has a narrower bandwidth, resulting in enhanced sensitivity and measurement accuracy.

The formula for calculating the quality factor is presented in Equation 5, where λ_0 denotes the resonance wavelength (in nanometers), and FWHM is the full width at half maximum (also in nanometers):

$$Q = \frac{\lambda_0}{FWHM} \tag{5}$$

The Detection Limit (DL) is a critical parameter that defines the smallest change in the refractive index that an optical sensor can reliably detect. It reflects the sensor's minimum measurable signal variation and is an important indicator of sensitivity in low-concentration environments. The DL is mathematically defined in Equation 6.

$$DL = \frac{\lambda_0}{10SQ} \tag{6}$$

2.4. Results of the proposed Sensor

Simulations were performed using RSoft Photonics CAD Suite (Version 8.2 RC5, RSoft Design Group; distributed by Keysight Technologies, USA) [38], employing the FullWAVE and BandSOLVE environments. The FullWAVE module utilizes the finite-difference time-domain (FDTD) method to solve Maxwell's equations, while BandSOLVE is used for photonic band structure calculations. In this study, the analysis was performed for three tissue types (Healthy Tissue (Reference), HPV-Infected (Pre-Cancerous) Tissue, and Cancerous Tissue), at temperatures of 10°C, 25°C, 45°C, and 60°C.

The FDTD method is well established and widely used for simulating 2D photonic crystal structures. In [39, 40], 2D photonic crystal structures were used as terahertz waveguides, and the FDTD simulation results matched the experimental measurements very closely. This agreement increases our confidence that the simulated performance of the proposed structure will carry over to practical experiments.

We used a uniform grid of 10 nm ($\Delta x = \Delta y = \Delta z = 0.01$ µm) to capture the photonic crystal details. To suppress unwanted reflections at the edges, we applied perfectly matched layers (PML) with a thickness of 0.5 µm. The time step was set to 0.001, which is below the stability limit (0.001227), ensuring numerical stability. The simulation ran for 10,000 time units to reach steady state. For convergence, we refined the grid to 5 nm; the resonance wavelength changed by less than 0.5 nm, confirming the accuracy and reliability of the results.

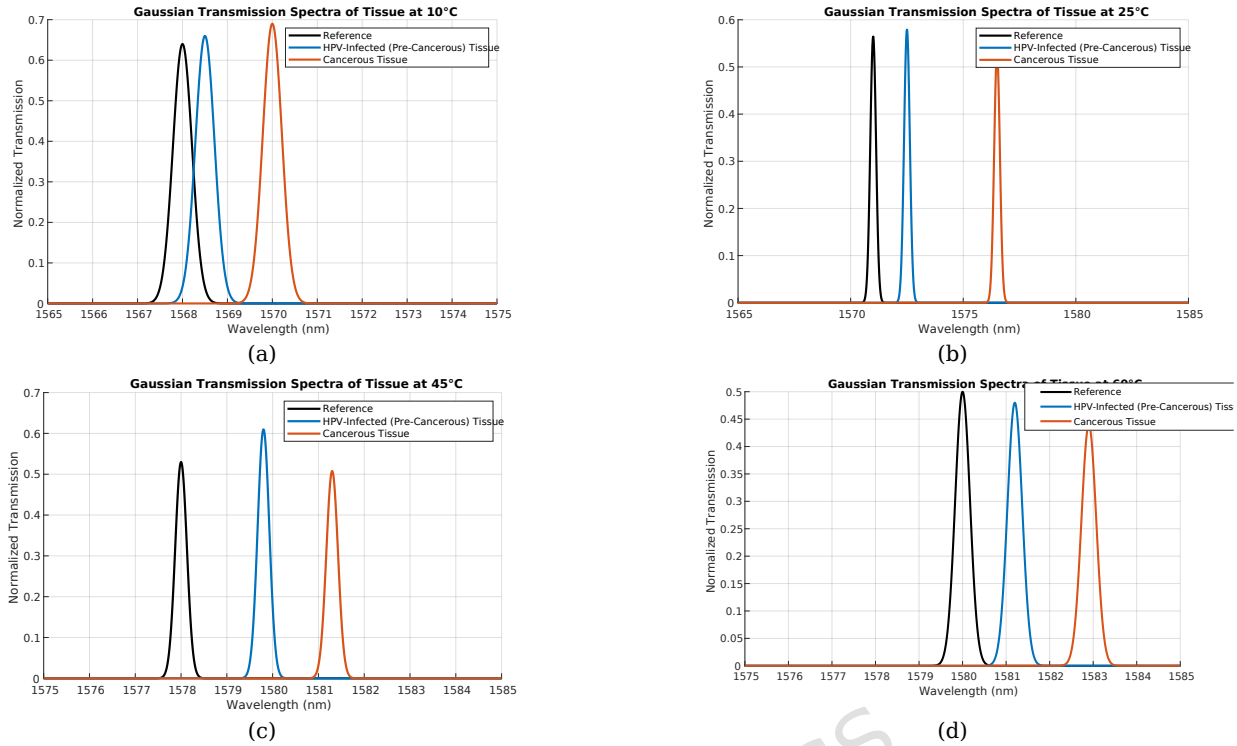

Figure 12. Normalized transmission spectra of three tissue types (healthy tissue (reference), HPV-infected (pre-cancerous) tissue, and cancerous tissue) at different temperatures. (a) 10°C, (b) 25°C, (c) 45°C, and (d) 60°C. In each case, the healthy tissue is used as the reference. As temperature increases, the resonance wavelength of both the HPV-Infected and Cancerous Tissues shifts to the right, with varying magnitudes.

Figure 12a shows the normalized transmission spectra of all three tissue types (healthy tissue (reference), HPV-infected (pre-cancerous) tissue, and cancerous tissue) at a temperature of 10°C. The healthy tissue is considered as the reference. As seen in Figure 12a, the resonance wavelength (λ_0) of the HPV-infected tissue has shifted by 0.5 μm and that of the cancerous tissue by 2 μm to the right. The FWHM of the waves is 0.5 nm. Figure 12b shows the normalized transmission spectra of all three tissue types at a temperature of 25°C. The resonance wavelength of the HPV-infected tissue has shifted by 1.5μm and that of the cancerous tissue by 5.5 μm to the right. The FWHM of the waves is 0.3 nm. Compared to the results at 10°C, this indicates a larger wavelength shift, which leads to increased sensor sensitivity at 25°C. Figure 12c presents the normalized transmission at a temperature of 45°C. As illustrated, the resonance wavelength exhibits a rightward shift of 1.8 μm, while the cancerous tissue shows a shift of 3.3 μm. The FWHM values for both spectra are 0.3 nm. Figure 12d shows the normalized transmission spectra at a temperature of 60°C. As shown, the λ_0 has shifted by 1.2 μm and that of the cancerous tissue by 2.9 μm to the right. The FWHM of the waves is 0.4 nm.

Figure 13a illustrates the sensor performance parameters i.e. sensitivity, FOM, DL, and (Q-F) at a temperature of 10°C for HPV-infected and cancerous tissues. For the HPV-infected tissue, the sensitivity, FOM, DL, and Q-F values are 2500 nm/RIU, 5000 RIU, 0.00002, and 3137, respectively. For the cancerous tissue, these values are 1818 nm/RIU, 6280 RIU, 0.000027, and 3140. Figure 13b presents the sensor parameters at a temperature of 25°C. For the HPV-Infected tissue, the sensitivity, FOM, DL, and Q-F are 3750 nm/RIU, 12500 RIU, 0.000008, and 5255, respectively.

For the cancerous tissue, these values are 3666 nm/RIU, 12220 RIU, 0.000008, and 5241. Figure 13c shows the sensor parameters at a temperature of 45°C. For the HPV-infected tissue, the sensitivity, FOM, DL, and Q-F are 3000 nm/RIU, 10000 RIU, 0.00001, and 5271, respectively. For the cancerous tissue, these values are 1571 nm/RIU, 5236 RIU, 0.000019, and 5266. Figure 13d presents the sensor parameters at a temperature of 60°C. For the HPV-infected tissue, the sensitivity, FOM, DL, and Q-F are 1714 nm/RIU, 4285 RIU, 0.000023, and 3957, respectively. For the cancerous tissue, these values are 1526 nm/RIU, 3815 RIU, 0.000026, and 3953.

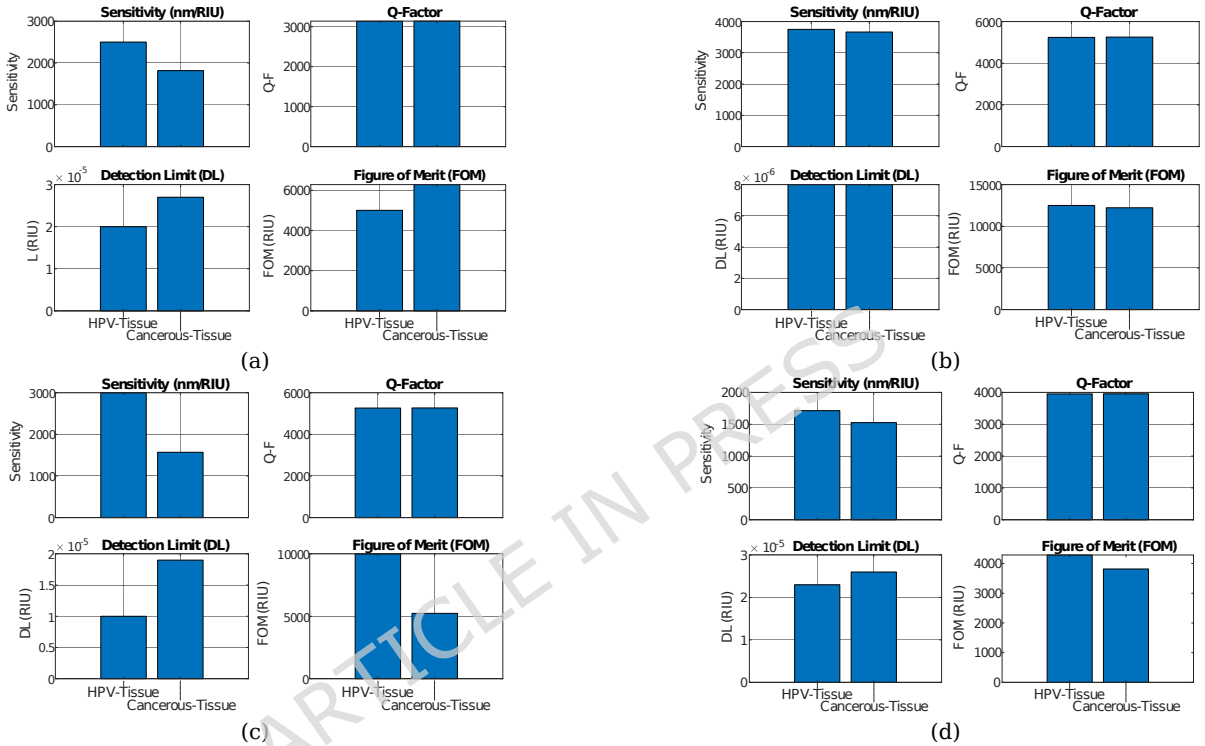

Figure 13. Sensor performance parameters, sensitivity, FOM, DL, and Q-F for HPV-Infected and cancerous tissues at temperatures of (a) 10°C, (b) 25°C, (c) 45°C, and (d) 60°C. Results show temperature-dependent variations, with peak sensitivity and FOM observed at 25°C for both tissue types.

Figure 14 shows the sensor performance parameters across 10°C, 25°C, 45°C, and 60°C temperatures, providing a comprehensive view of the impact of temperature on sensor performance. As seen in the figure, the highest sensitivity is observed at 25°C, the highest quality factor (Q-F) at 45°C, the highest FOM at 25°C, and the lowest detection limit (DL) at 25°C.

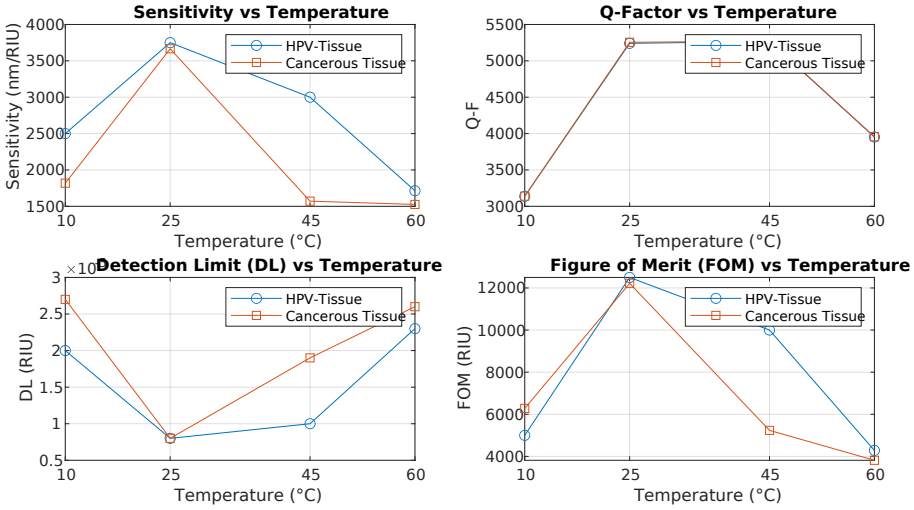

Figure 14. Graphs of Sensitivity, FOM, DL, and Q-F parameters at temperatures of 10°C, 25°C, 45°C, and 60°C.

Table 3 presents the values of the optical sensor parameters provided in this study, including the refractive index difference (Δ_n), the resonance wavelength shift (Δ_λ) measured for the analyzed materials compared to the reference resonance wavelength, resonance wavelength (λ_0), FWHM (nm), Q-F, sensitivity (nm/RIU), FOM (nm/RIU), and the DL at different temperatures for all three tissue types. Although the sensor's best performance was observed at 25°C, the results show that at temperatures near the physiological 37°C, the sensitivity and Q-factor are maintained with less than 10% reduction. This indicates that the sensor has suitable thermal stability within the temperature range relevant to the human body.

Table 3. Summary of optical sensor parameters for healthy, HPV-infected, and cancerous tissues at different temperatures 10°C, 25°C, 45°C, And 60°C.

DL≅	FOM (RIU)	Sensitivity (nm/RIU)	Q-F	*FWHM* (nm)	Δλ	γ_0 (nm)	Δn	n	Tem (℃)	Tissue Type
-	-	-	3136	0.5	-	1568	-	1.3438	10	Healthy Tissue (Reference)
0.00002	5000	2500	3137	0.5	0.5	1568.5	0.0002	1.3440	10	HPV-Tissue
0.00027	6280	1818	3140	0.5	2	1570	0.0011	1.3449	10	Cancerous Tissue
-	-	-	5236	0.3	-	1571	-	1.3456	25	Healthy Tissue (Reference)
0.000008	12500	3750	5241	0.3	1.5	1572.5	0.0004	1.3460	25	HPV-Tissue
0.000008	12220	3666	5255	0.3	5.5	1576.5	0.0015	1.3471	25	Cancerous Tissue
-	-	-	5260	0.3	-	1578	-	1.3480	45	Healthy Tissue (Reference)
0.00001	10000	3000	5266	0.3	1.8	1579.8	0.0006	1.3486	45	HPV-Tissue
0.00019	5236	1571	5271	0.3	3.3	1581.3	0.0021	1.3501	45	Cancerous Tissue
-	-	-	3950	0.4	-	1580	-	1.3498	60	Healthy Tissue (Reference)
0.00023	4285	1714	3953	0.4	1.2	1581.2	0.0007	1.3505	60	HPV-Tissue
0.00026	3815	1526	3957	0.4	2.9	1582.9	0.0019	1.3524	60	Cancerous Tissue

As shown in Table 4, the sensitivity and Q-F parameters of the proposed optical sensor are higher than all the recent comparative works. The FOM is significantly greater than those in previous

studies, and the detection limit (DL) is considerably lower than earlier designs. Additionally, the compact size and structural simplicity of the proposed design make it suitable for integration into on-chip circuits. The consideration of temperature effects on sensor performance further enhances its practicality. Altogether, these features make the proposed optical sensor a strong candidate for effective cervical cancer detection. The superior Q-factor and FOM reported for our design in Table 4 arise from an optimized cavity with a small mode volume, strong light–matter overlap in the sensing region, and the high refractive-index contrast between silicon and the analyte. These features produce a larger resonance wavelength shift and a very narrow bandwidth (FWHM ≈ 0.3 nm), which directly increases both Q and FOM. We note, however, that these values were obtained under ideal simulation conditions and may be lower in practice; fabrication tolerances can also introduce deviations between experimental and simulated results.

Table 4. Comparison of the proposed photonic crystal sensor with previous works.

Footprint (μm^2)	DL (RIU^{-1})	FOM ($\frac{nm}{RIU}$)	Sensitivity ($\frac{nm}{RIU}$)	Q-F	Sensor Type	Temp.Cons.	Ref	Year
99	0.003		1170	423	2D-PC	no	[41]	2023
156	-	1400	690	2500	2D-PC	no	[42]	2018
120	0.002	-	-	262	2D-PC	no	[43]	2019
-	1.44	-	546.72	2066.44	2D-PC	no	[44]	2020
-	-	-	74.5	19.82	1D-PC	no	[45]	2021
-	-	-	203.09	1569	1D-PC	no	[46]	2022
-	-	104	428.6	104	1D-PC	no	[47]	2022
234	0.021	9.84	2.94	5166	2D-PC	no	[48]	2022
248	0.0024	70.7	72.28	5255	2D-PC	no	[49]	2024
-	0.000204	488	1350	600	2D-PC	no	[50]	2021
-	0.00016	737	600	2081	2D-PC	no	[51]	2019
123	-	593.9	756.1	1092	2D-PC	no	[52]	2023
90	-	888	324	3690	2D-PC	no	[53]	2023
-	0.000236	-	915.75	980	2D-PC	no	[54]	2023
51.32	0.0000043	22,856.7	457.1	54,669	2D-PC	no	[22]	2025
48	0.01	159.54	15,085	81.58	2D-PC	no	[21]	2022
168	0.000498	201.3	3582.7	52.88	2D-PC	no	[25]	2025
87	0.00000587	-	1738.7	10731	2D-PC	no	[55]	2023
43	0.00000908	-	1332	16254	2D-PC	no	[56]	2023
225	0.00057	181.5	1964.3	117	2D-PC	no	[57]	2025
72	0.00024	216	899	711	2D-PC	no	[58]	2025
18.95	0.00021	_	670	1053	2D-PC	no	[59]	2025
120	0.000008	12500	3750	5271	2D-PC	yes	This work	2025

3. ANN-Based Tissue Classification

To explore the potential for automatic classification, we used an artificial neural network (ANN) to classify tissue types based on the sensor outputs. Three features are considered to train the model which are the wavelength shift (Δλ), the width of the response curve (FWHM), and the temperature at which the data was taken. The proposed ANN goal is to classify each sample as either healthy, HPV-infected, or cancerous. The proposed ANN is trained using a small dataset of 12 simulated samples. The network had two hidden layers with 16 and 8 neurons, respectively, and used standard techniques to optimize learning.

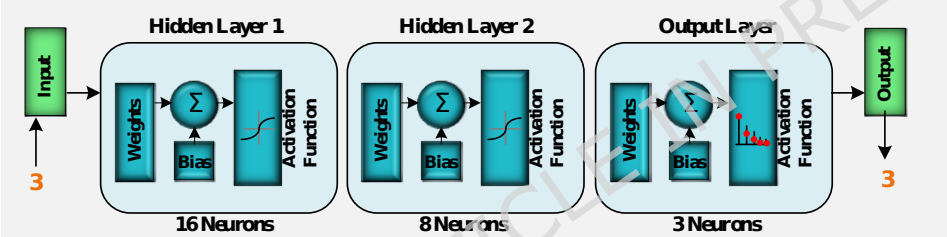

Figure 15. Structure of the proposed ANN model, designed for tissue classification based on optical sensor inputs.

Figure 15 illustrates the architecture of the proposed ANN, used for classifying tissue types based on three input features. The network comprises two hidden layers with 16 and 8 neurons respectively, each applying a tangent sigmoid activation function to introduce nonlinearity. The final output layer consists of three neurons corresponding to the three tissue categories: Healthy, HPV-infected, and Cancerous, using a softmax activation function to enable multi-class classification.

The ANN achieved an average classification accuracy of 91.7%. It correctly identified all cancerous tissue samples, and most of the healthy and HPV samples. The only confusion occurred between healthy and HPV-infected tissues, which have similar optical characteristics. We also calculated precision, recall, and F1-score for each class to ensure a balanced evaluation of the model's performance. These results suggest that combining our sensor with a neural network could help enable intelligent, real-time diagnosis in future implementations. The confusion matrix of the proposed ANN classifier for tissue type detection using sensor output parameters is shown in Figure 16a.

Figure 16. Confusion matrix of the neural network classifier for tissue type detection using sensor output parameters. The matrix compares predicted classes (vertical axis) against true labels (horizontal axis). Class 1 = Healthy, Class 2 = HPV-infected, Class 3 = Cancerous. (a) Original dataset, and (b) augmented dataset.

Table 5. Final performance metrics of the proposed ANN used for tissue classification based on optical sensor inputs.

Class	Precision (%)	Recall (%)	F1-Score (%)
Healthy Tissue (Class 1)	100.0	80.0	88.9
HPV-Infected Tissue (Class 2)	75.0	100.0	85.7
Cancerous Tissue (Class 3)	100.0	100.0	100.0
Macro Average	91.7	93.3	91.5
Overall Accuracy	91.7%		

Table 5 summarizes the classification performance of the ANN across three tissue types: Healthy, HPV-Infected, and Cancerous. Precision, recall, and F1-score are reported per class, along with macro-averaged values to provide an overall view of model performance. The ANN achieved a high overall accuracy of 91.7%, with particularly strong performance in identifying cancerous tissues.

Since the obtained dataset is small, data augmentation is performed by introducing small noise into the existing measurements. The data is dataset expanded by a factor of 10, generating a total of 120 rows. This was achieved by adding Gaussian noise with a mean of 0 and a standard deviation of 1% to each numerical feature, including the wavelength shift, FWHM, and temperature values, while preserving the original tissue class labels. After augmenting the dataset, the model achieved 100% accuracy in classifying tissue types. This is expected, as the noise added during augmentation was small enough to preserve the underlying patterns in the data, allowing the model to better distinguish between the tissue classes. The augmentation helped the model generalize well without overfitting, leading to a perfect classification performance. The confusion matrix of the proposed ANN classifier for augmented dataset is shown in Figure 16b.

4. Conclusions

In this study, we designed and simulated a compact, label-free optical biosensor based on a two-dimensional photonic crystal structure for early detection of cervical cancer. The sensor operates at a wavelength of 1.55 μm and demonstrates high sensitivity, precision, and temperature stability. By accounting for temperature

effects, we showed that even small changes in refractive index, caused by healthy, HPV-infected, or cancerous tissues, can be accurately detected. The obtained results highlight the sensor's strong performance across a range of conditions, with peak sensitivity and figure of merit observed at 25°C. Thanks to its simple structure, ease of integration, and excellent detection capabilities, the proposed sensor is a promising tool for non-invasive, real-time medical diagnostics, especially for cervical cancer screening. To further validate the sensor output data and enable automated tissue classification, an artificial neural network (ANN) was applied. Using inputs such as wavelength shift, FWHM, and temperature, the ANN achieved a classification accuracy of 91.7% across three tissue types.

It should be noted that future experimental validation will be needed to confirm the simulation results. Finally, we emphasize that the proposed sensor, in its current form, is a refractive-index–based detector without selective molecular binding; therefore, the findings should be regarded as a proof of concept. Developing suitable surface functionalization will be essential for practical clinical use, and we believe this work can help advance clinical optical biosensors.

Data Availability Statement

The corresponding author can be contacted on reasonable request.

Author Contributions Statement

P.K., S.I.Y., Sa.R, and F.P. designed the sensor model and performed the simulations. F.P. and So.R contributed to the neural network modeling and data analysis. P.K. and Sa.R. wrote the main manuscript text. S.I.Y. prepared the figures and visualizations. All authors contributed equally to the research, discussed the results, and reviewed the manuscript.

Funding

The authors declare that no funding was received for this research or the publication of the article.

References

[1] E. T. Fontham *et al.*, "Cervical cancer screening for individuals at average risk: 2020 guideline update from the American Cancer Society," *CA: a cancer journal for clinicians,* vol. 70, no. 5, pp. 321-346, 2020.

[2] F. X. Bosch *et al.*, "Prevalence of human papillomavirus in cervical cancer: a worldwide perspective," *JNCI: Journal of the National Cancer Institute,* vol. 87, no. 11, pp. 796-802, 1995.

[3] K. A. Kundrod, C. A. Smith, B. Hunt, R. A. Schwarz, K. Schmeler, and R. Richards-Kortum, "Advances in technologies for cervical cancer detection in low-resource settings," *Expert review of molecular diagnostics,* vol. 19, no. 8, pp. 695-714, 2019.

[4] M. Azadi, M. Mohammadi, S. Olyaee, and M. Seifouri, "Design and simulation of a D-shaped plasmonic biosensor utilizing dual-core photonic crystal fiber," *Plasmonics,* pp. 1-8, 2025.

[5] F. Parandin, F. Heidari, Z. Rahimi, and S. Olyaee, "Two-Dimensional photonic crystal Biosensors: A review," *Optics & laser technology,* vol. 144, p. 107397, 2021.

[6] A. Sundhar, R. Valli, S. Robinson, A. Abinayaa, and C. SivaBharathy, "Two dimensional photonic crystal based bio sensor for cancer cell detection," in *2019 IEEE international conference on system, computation, automation and networking (ICSCAN)*, 2019: IEEE, pp. 1-3.

[7] M. Z. Elabdein, O. E. Khedr, N. A. Mohammed, and E.-S. M. El-Rabaie, "Recent advances in photonic crystal fiber based chemical and industrial sensors: a review," *Journal of Optics,* pp. 1-19, 2024.

[8] O. E. Khedr *et al.*, "Emerging trends in photonic crystal on-chip sensors for biomedical applications: a review," *Journal of Optics,* pp. 1-18, 2025.

[9] F. Bagheri and M. Soroosh, "Design and simulation of subwavelength plasmonic D flip-flop with state remaining feature," *Optical and Quantum Electronics,* vol. 55, no. 5, p. 425, 2023.
[10] P. Karami *et al.*, "Design of a photonic crystal exclusive-OR gate using recurrent neural networks," *Symmetry,* vol. 16, no. 7, p. 820, 2024.
[11] F. Parandin, P. Karami, and A. Mohamadi, "Machine learning-driven optimization of photonic crystal structures for superior optical NOR gate performance," *Applied Optics,* vol. 63, no. 25, pp. 6666-6673, 2024.
[12] M. Soroosh, F. Parandin, F. Haddadan, M. Maleki, and F. Bagheri, "Highly efficient materials for photonic crystal-based optical components," in *Advances in All-Optical Communication*: IOP Publishing Bristol, UK, 2024, pp. 1-1-1-20.
[13] P. Karami *et al.*, "Advancing optical neural networks: photonic crystal perceptrons for ultra-fast AI computing," *Optics Continuum,* vol. 4, no. 8, pp. 1810-1825, 2025.
[14] F. Heidari, D. Pashabadi, M. Fathi, and M. Razaghi, "Optical XOR logic gate design in two dimensional photonic crystal using ANN and PSO," *Scientific Reports,* vol. 15, no. 1, p. 26471, 2025.
[15] A. K. Pradhan, C. Prakash, T. Datta, M. Sen, and H. Mondal, "ANN-based estimation of dispersion characteristics of slotted photonic crystal waveguides," *Journal of Computational Electronics,* vol. 23, no. 3, pp. 552-560, 2024.
[16] V. Fallahi, Z. Kordrostami, and M. Hosseini, "Cancer detection by photonic crystal optical biosensors: Effect of hexagonal micro ring resonator design," *Materials Science in Semiconductor Processing,* vol. 174, p. 108188, 2024.
[17] D. Kundu *et al.*, "High sensitivity cervical cancer detection employing hollow decagonal core photonic crystal fiber in the Terahertz Region," *Applied Physics A,* vol. 131, no. 2, pp. 1-13, 2025.
[18] F. Jin *et al.*, "A simple and integrated fiber-optic real-time qPCR platform for remote and distributed detection of epidemic virus infection," *Biosensors and Bioelectronics,* vol. 273, p. 117145, 2025.
[19] S. Vardhan, D. Srivastava, N. K. Gupta, R. R. Singh, and S. Kumar, "Spectral Envelope Analysis of Subwavelength Grating Waveguide Micro Racetrack Ring Resonator for Cancer Sensing Using Integrated Photonics," in *Photonics*, 2025, vol. 12, no. 4: MDPI, p. 376.
[20] H. Sharifi and S. Eskandari, "Sensing blood components and cancer cells with photonic crystal resonator biosensor," *Results in Optics,* vol. 14, p. 100593, 2024.
[21] H. Miyan, R. Agrahari, S. K. Gowre, M. Mahto, and P. K. Jain, "Computational study of a compact and high sensitive photonic crystal for cancer cells detection," *IEEE Sensors Journal,* vol. 22, no. 4, pp. 3298-3305, 2022.
[22] O. E. Khedr, N. A. Mohammed, E.-S. M. El-Rabaie, and A. A. Khalaf, "Advanced on-chip photonic sensors for malignancy biomarker detection using tunable nanostructures," *Optical and Quantum Electronics,* vol. 57, no. 8, p. 454, 2025.
[23] M. Z. Elabdein, N. A. Mohammed, E.-S. M. El-Rabaie, and O. E. Khedr, "Highly precise optical detection of mass destruction nerve agents based on photonic crystal fibers," *Scientific Reports,* vol. 15, no. 1, p. 32609, 2025.
[24] O. E. Khedr, N. M. Saad, E. M. ElRabaie, and A. A. Khalaf, "Early diagnosis of Chikungunya virus utilizing square core photonic crystal fiber (SC-PCF) with extremely high relative sensitivity," *Optical and Quantum Electronics,* vol. 56, no. 9, p. 1464, 2024.
[25] E. Rafiee, "Bio-sensing applications of a 2: 1 photonic crystal multiplexer," *Scientific Reports,* vol. 15, no. 1, p. 16840, 2025.
[26] M. B. Hossain and E. Podder, "Design and investigation of PCF-based blood components sensor in terahertz regime," *Applied Physics A,* vol. 125, no. 12, p. 861, 2019.
[27] E. Podder, M. B. Hossain, R. H. Jibon, A. A.-M. Bulbul, and H. S. Mondal, "Chemical sensing through photonic crystal fiber: sulfuric acid detection," *Frontiers of Optoelectronics,* vol. 12, no. 4, pp. 372-381, 2019.
[28] R. H. Jibon, E. Podder, M. E. Rahaman, B. Hossain, and K. Ahmed, "Design and investigation of a novel photonic crystal fiber sensor for detecting human body protein: amino acids of different types," *Sensing and Imaging,* vol. 25, no. 1, p. 65, 2024.
[29] M. B. Hossain, J. Kříž, V. Dhasarathan, and M. E. Rahaman, "Photonic crystal fiber (PhCF) for petrochemical sensing," *Frontiers in Physics,* vol. 10, p. 1097841, 2023.
[30] H. Monshat *et al.*, "Integration of nucleic acid amplification, detection, and melting curve analysis for rapid genotyping of antimicrobial resistance," *IEEE Sensors Journal,* vol. 22, no. 8, pp. 7534-7541, 2022.

[31] F. Parandin and P. Karami, "Numerical analysis of All-Optical universal NAND and NOR photonic crystal logic gates by creating holes in silicon material," *Optics & Laser Technology,* vol. 182, p. 112197, 2025.
[32] P. Karami, A. Mohamadi, and F. Parandin, "Enhancing integrated optical circuits: optimizing all-optical NAND and NOR gates through deep learning and machine learning," *Optical and Quantum Electronics,* vol. 57, no. 1, p. 73, 2024.
[33] K. Ahmed, B. K. Paul, F. Ahmed, M. A. Jabin, and M. S. Uddin, "Numerical demonstration of triangular shaped photonic crystal fibre-based biosensor in the Terahertz range," *IET Optoelectronics,* vol. 15, no. 1, pp. 1-7, 2021.
[34] M. A. Jabin *et al.*, "Surface plasmon resonance based titanium coated biosensor for cancer cell detection," *IEEE Photonics Journal,* vol. 11, no. 4, pp. 1-10, 2019.
[35] P. Kumar, V. Kumar, and J. S. Roy, "Dodecagonal photonic crystal fibers with negative dispersion and low confinement loss," *Optik,* vol. 144, pp. 363-369, 2017.
[36] T. Parvin, K. Ahmed, A. M. Alatwi, and A. N. Z. Rashed, "Differential optical absorption spectroscopy-based refractive index sensor for cancer cell detection," *Optical Review,* vol. 28, pp. 134-143, 2021.
[37] P. Sharma, P. Sharan, and P. Deshmukh, "A photonic crystal sensor for analysis and detection of cancer cells," in *2015 International conference on pervasive computing (ICPC)*, 2015: IEEE, pp. 1-5.
[38] "Keysight Technologies. RSoft CAD Environment. Available at:." https://www.keysight.com/us/en/products/software/optical-solutions-software/photonic-design-solutions/rsoft-cad-environment.html (accessed Feb. , 2026).
[39] S. D. A. Shah, H. Li, B. Kuhlmey, and S. Atakaramians, "3D printed horn coupler for hybrid photonic crystal THz waveguides," in *2021 46th International Conference on Infrared, Millimeter and Terahertz Waves (IRMMW-THz)*, 2021: IEEE, pp. 1-2.
[40] M. Sun, H. Lees, and W. Withayachumnankul, "All-Dielectric Tapered Rod Antenna with Sub-Wavelength Grating for Terahertz Waves," *IEEE Antennas and Wireless Propagation Letters,* 2025.
[41] M. H. Jokar, A. Naraghi, M. Seifouri, and S. Olyaee, "Photonic crystal bio-sensor for highly sensitive label-free detection of cancer cells," *Optical and Quantum Electronics,* vol. 55, no. 7, p. 660, 2023.
[42] A. Tavousi, M. Rakhshani, and M. Mansouri-Birjandi, "High sensitivity label-free refractometer based biosensor applicable to glycated hemoglobin detection in human blood using all-circular photonic crystal ring resonators," *Optics Communications,* vol. 429, pp. 166-174, 2018.
[43] R. Arunkumar, T. Suaganya, and S. Robinson, "Design and analysis of 2D photonic crystal based biosensor to detect different blood components," *Photonic Sensors,* vol. 9, pp. 69-77, 2019.
[44] M. Maache, Y. Fazea, I. Bile Hassan, A. A. Alkahtani, and I. Ud Din, "High-sensitivity capsule-shaped sensor based on 2D photonic crystals," *Symmetry,* vol. 12, no. 9, p. 1480, 2020.
[45] A. Bijalwan, B. K. Singh, and V. Rastogi, "Analysis of one-dimensional photonic crystal based sensor for detection of blood plasma and cancer cells," *Optik,* vol. 226, p. 165994, 2021.
[46] S. Sharma and A. Kumar, "Design of a biosensor for the detection of dengue virus using 1D photonic crystals," *Plasmonics,* vol. 17, no. 2, pp. 675-680, 2022.
[47] Z. Matar, M. Al-Dossari, S. Awasthi, D. Mohamed, N. Abd El-Gawaad, and A. Aly, "Conventional biophotonic sensing approach for sensing and detection of normal and infected samples containing different blood components," *Crystals,* vol. 12, no. 5, p. 650, 2022.
[48] F. Parandin, F. Heidari, M. Aslinezhad, M. M. Parandin, S. Roshani, and S. Roshani, "Design of 2D photonic crystal biosensor to detect blood components," *Optical and Quantum Electronics,* vol. 54, no. 10, p. 618, 2022.
[49] Z. Rahimi, F. Parandin, S. Roshani, and S. Roshani, "Design of 2D photonic crystal biosensor to detect cancer cells," *Journal of Optics,* pp. 1-11, 2024.
[50] L. Hajshahvaladi, H. Kaatuzian, and M. Danaie, "Design of a hybrid photonic-plasmonic crystal refractive index sensor for highly sensitive and high-resolution sensing applications," *Physics Letters A,* vol. 420, p. 127754, 2021.
[51] F. Rahman-Zadeh, M. Danaie, and H. Kaatuzian, "Design of a highly sensitive photonic crystal refractive index sensor incorporating ring-shaped GaAs cavity," *Opto-Electronics Review,* vol. 27, no. 4, pp. 369-377, 2019.
[52] V. Fallahi, Z. Kordrostami, and M. Hosseini, "A solution for detection of ethanol and methanol with overlapping refractive indexes based on photonic crystal ring resonator optical sensors," *IEEE Sensors Journal,* vol. 23, no. 7, pp. 6791-6798, 2023.

[53] F. Baraty and S. Hamedi, "Label-Free cancer cell biosensor based on photonic crystal ring resonator," *Results in Physics,* vol. 46, p. 106317, 2023.
[54] Y. Yang, Y. Xiang, and X. Qi, "Design of photonic crystal biosensors for cancer cell detection," *Micromachines,* vol. 14, no. 7, p. 1478, 2023.
[55] N. A. Mohammed, O. E. Khedr, E.-S. M. El-Rabaie, and A. A. Khalaf, "Tuberculosis biomedical sensor based on on-chip nanocavity 2D photonic crystal with high sensitivity and quality factor," *Measurement,* vol. 222, p. 113595, 2023.
[56] N. A. Mohammed, O. E. Khedr, E.-S. M. El-Rabaie, and A. A. Khalaf, "Brain tumors biomedical sensor with high-quality factor and ultra-compact size based on nanocavity 2D photonic crystal," *Alexandria Engineering Journal,* vol. 64, pp. 527-540, 2023.
[57] E. Rafiee, "1: 4 D-multiplexer based on photonic crystal configuration for detection of biological elements," *Optical and Quantum Electronics,* vol. 57, no. 6, p. 365, 2025.
[58] S. Alam, M. M. Khan, and R. K. Sonkar, "Dengue disease detection via a minimal area 2D photonic crystal nanocavity-based refractive index optical biosensor: numerical analysis," *Applied Optics,* vol. 64, no. 16, pp. 4615-4624, 2025.
[59] K. M. Abohassan, "Side-Coupled Microcavity Biosensor for Detection of Blood Components," *Sensing and Imaging,* vol. 26, no. 1, p. 14, 2025.